Materials Science & Engineering A 855 (2022) 143911

Contents lists available at ScienceDirect

Materials Science & Engineering A

journal homepage: www.elsevier.com/locate/msea

# Mechanical behavior of freeze-cast Ti foams with varied porosity

Péter Jenei [a], Csilla Kádár [b,c], Ábel Szabó [a], Sun–Mao Hung [d], Chia–Jung Kuo [d], Heeman Choe [e], Jenő Gubicza [a,*]

[a] Department of Materials Physics, Eötvös Loránd University, Budapest, P.O.B. 32, H-1518, Hungary
[b] Department of Materials Science and Engineering, Budapest University of Technology and Economics, Műegyetem rakpart 3, H-1111 Budapest, Hungary
[c] MTA–BME Lendület Composite Metal Foams Research Group, Műegyetem rakpart 3.,H-1111, Budapest, Hungary
[d] CellMobility Inc., 11F, Sec.4, Nanjin E. Rd., Taipei, China
[e] School of Materials Science and Engineering, Kookmin University, 77 Jeongneung-ro, Seongbuk-gu, Seoul, 02707, Republic of Korea

ARTICLE INFO

*Keywords:*
Titanium foam
Freeze casting
Porosity
Compression
Strength

ABSTRACT

Titanium (Ti) foams with relative densities of 0.32, 0.37, and 0.49 were processed via freeze casting. The mechanical characteristics of samples with different porosities were studied in uniaxial compression tests at initial strain rates between 0.001 and 0.5 $s^{-1}$. According to the results, the stress–strain response does not significantly depend on the strain rate, at least up to the applied maximum stress, which corresponds to 0.1–0.3 engineering strain. In-situ acoustic emission (AE) experiments have revealed that the stress drop beyond the maximum stress corresponds to the formation and propagation of macrocracks. However, cracks were also initiated below the maximum stress, particularly, in samples with higher relative densities. The analysis of the Young's modulus and yield strength versus the porosity exhibits a power law relationship with a high exponent (approximately 4–5). This high exponent is reasonable if the decrease in the porosity level is associated with a change in the deformation mechanism from the compression model to the Gibson–Ashby (GA) model between 0.37 and 0.49 relative density.

## 1. Introduction

Engineers have created various porous metallic materials (i.e., foams) from almost all common metals such as Al, Cu, and Fe with cubic crystal structures or hexagonal Mg and Ti [1–3]. Foams made of Ti and its alloys are important because they can be used as biomedical implant materials in surgery [4,5] and as sandwich panel cores for aircraft bodies and floors in the aerospace industry [6,7]. Regarding the former case, the biocompatibility of Ti and its high strength due to the hexagonal crystal structure are two important features that predestine it for surgical applications. The high strength and mechanical stability of Ti foams at elevated temperatures make them suitable structural materials in the aerospace industry. Moreover, the mechanical performance of Ti foams can be enhanced with an auxetic pore structure [8,9]. This structure has a negative Poisson's ratio, which increases the resistance of the material against deformations caused by external mechanical forces and improves its absorption properties [9].

Researchers have developed different methods for processing Ti foams [7], such as the space-holder technique [10–15], diffusion bonding [16], the application of blowing agents [17], and freeze casting [18–22]. The two most prevailing techniques are the space holder and freeze casting methods to produce Ti foams. The advantage of the former process over other processes is its great designability. A large variety of foam microstructures can be obtained through the selection of the space holder size and shape; thus, the microstructure–property relationship can be easily investigated [3]. Freeze casting is also a flexible procedure; the porosity, pore size, pore shape, and orientation can be tuned by changing the characteristics of the suspension. However, owing to the complexity of the templating mechanism, determining the relationship among the microstructure, property, and processing conditions is rather difficult [1].

In all applications of Ti foams, the load bearing capacity is a very important feature. Researchers have mainly studied the porosity dependence of the Young's modulus and compressive strength [10–23]. To describe the relationship between the relative density and strength or modulus, researchers usually use power law functions in accordance with the model calculations [24]. Owing to the large variability of the microstructures of Ti foams processed with different methods, the

* Corresponding author.
*E-mail address:* jeno.gubicza@ttk.elte.hu (J. Gubicza).

https://doi.org/10.1016/j.msea.2022.143911
Received 27 June 2022; Received in revised form 25 August 2022; Accepted 27 August 2022
Available online 5 September 2022

parameters of these functions can differ for different sample series. For instance, the power law exponent of the relative strength–relative density relationship of different Ti foam series varies between 1 and 5 [10–15]. As suggested by its different values calculated from different deformation models, this exponent is a fingerprint of the deformation mechanisms. For instance, in the cases of the compression and Gibson–Ashby (GA) models, the exponent values characterizing the density–strength relationship are 1 and 1.5, respectively [1,23,24]. It should be noted that there is no model in literature that can explain the experimentally observed high values (4–5) for the power law exponents in the strength–density and modulus–density relationships. Therefore, the origin of this effect must be determined in additional studies.

In this study, the compression behavior of Ti foams with 0.32–0.49 relative density processed via freeze casting was investigated. More specifically, the effects of the porosity and strain rate of compression on the elastic modulus, yield strength, and maximum strain until failure were studied. Complementary acoustic emission (AE) experiments were conducted to reveal the deformation mechanisms. In this paper, the relationship between the mechanical behavior and porosity is discussed in detail, and an explanation is proposed for the high (4–5) power law exponents that were discovered in the experimentally determined strength–density and modulus–density relationships.

## 2. Experimental materials and methods

### 2.1. Sample processing

The Ti foams were processed via freeze casting (a schematic of the applied apparatus can be seen in Ref. [25]). First, 0.28 g poly(vinyl alcohol) (Mw 89,000–98,000; approximately 99% purity; manufacturer: Sigma-Aldrich Co., MO, USA) was dissolved in 10 mL distilled water; in the next step, 11.25 g Ti powder (Alfa Aesar, MA, USA) was added to the solution. The mixture was poured onto a Cu chiller rod standing in liquid $N_2$; the temperature of the rod was maintained at −50 °C. The frozen solution was lyophilized to remove ice through sublimation at −90 °C at $5 \times 10^{-3}$ Torr for approximately 20 h (Operon, OPR-FDU-7003, Republic of Korea). The lyophilized sample was sintered in a vacuum furnace. The final relative densities of the samples were determined by the sintering conditions.

Subsequently, the sample density was calculated by dividing the mass by the volume determined as the product of the edge dimensions of the rectangular specimens. The relative density was calculated as the ratio of the density of the foam and theoretical density of Ti (4.506 g $cm^{-3}$). The three prepared foams with different relative densities are shown in Table 1: the densities were approximately 0.49, 0.37, and 0.32. The samples are denoted as follows: Ti-0.49, Ti-0.37, and Ti-0.32, respectively. Furthermore, the sintering temperature and time were increased from 850 to 1000 °C and from 4 to 6 h depending on the desired relative density, respectively.

### 2.2. Microstructure characterization

The phase compositions of the samples were studied with X-ray diffraction equipped with a Smartlab X-ray diffractometer (manufacturer: Rigaku, Japan) using CuKα radiation (wavelength: λ = 0.15418 nm) in the Bragg–Brentano geometry.

The pore and grain structures of the specimens were investigated with an optical microscope (OM), scanning electron microscope (SEM), and electron backscatter diffraction (EBSD). The microstructures of the materials were examined with optical microscopy; for this step, cross-sections of the epoxy-filled specimens were polished with SiC paper and a polishing cloth. For the EBSD and SEM measurements, the foam surface was prepared with a focused ion beam (FIB) using Ga ions in the SEM. The incision was made along the edge of the sample (6° incidence angle). Before ion milling the two sides meeting at the given edge, they were mechanically polished with P1000, P2500, and P4000 grinding papers.

**Table 1**
Relative density and area-weighted mean grain size according to EBSD measurement results.

| Sample | Relative density | Grain size (μm) |
|---|---|---|
| Ti-0.49 | 0.490 ± 0.002 | 10.6 ± 4.1 |
| Ti-0.37 | 0.365 ± 0.002 | 6.4 ± 3.6 |
| Ti-0.32 | 0.316 ± 0.002 | 5.1 ± 2.5 |

### 2.3. Mechanical test

The Ti foam specimens with different porosities [51% (Ti-0.49), 63% (Ti-0.37), and 68% (Ti-0.32)], $3 \times 3$ $mm^2$ cross-sections, and 6 mm lengths were examined in uniaxial compression tests with an MTS810 (MTS Systems Corporation, Eden Prairie, MN, USA). Three different crosshead velocities corresponding to 0.001, 0.01, and 0.5 $s^{-1}$ initial strain rates at ambient temperature were applied during the compression tests. At least two specimens were examined for each porosity and crosshead velocity. The displacement was measured with an extensometer. Simultaneously, the AE response and deformation of the surface were recorded. To monitor the AE activity, a Vallen AMSY-6 system (Vallen Systeme GmbH, Icking, Germany) with a PAC Micro30S broadband sensor (Physical Acoustics, Princeton Junction, USA) and an AEP5 pre-amplifier (Vallen Systeme GmbH, Icking, Germany) that provides 40 dB gain were used in the streaming mode with a 1 MHz sampling rate. The sensor was attached to a waveguide. Finally, the investigated AE parameters were calculated by post-processing the AE data and applying a 0.07 mV threshold.

## 3. Results

### 3.1. Microstructure

Fig. 1 shows the XRD pattern of the Ti-0.32 foam. Only the peaks of the hexagonal close-packed (hcp) α-Ti are visible, thereby indicating that the sample did not contain other phases (e.g., oxide). Similar observations were made for the other two Ti foams.

The microstructures of the foams are shown in the optical and SEM images in Fig. 2. With increasing porosity, the number of neighbor contacts of the struts decreased significantly, which most probably weakened the structure. The sizes and morphologies of the grains inside the struts of the Ti foams with three different porosities can be seen in the EBSD images of Fig. 3. Table 1 shows that with decreasing relative

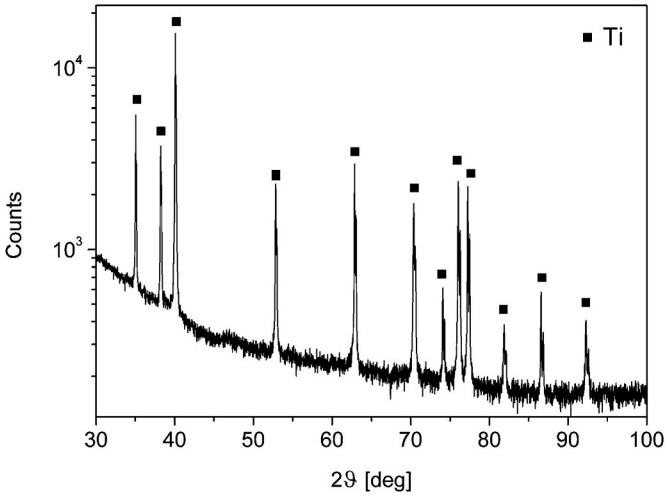


**Fig. 1.** X-ray diffractogram of Ti-0.32 sample with logarithmic intensity scale.

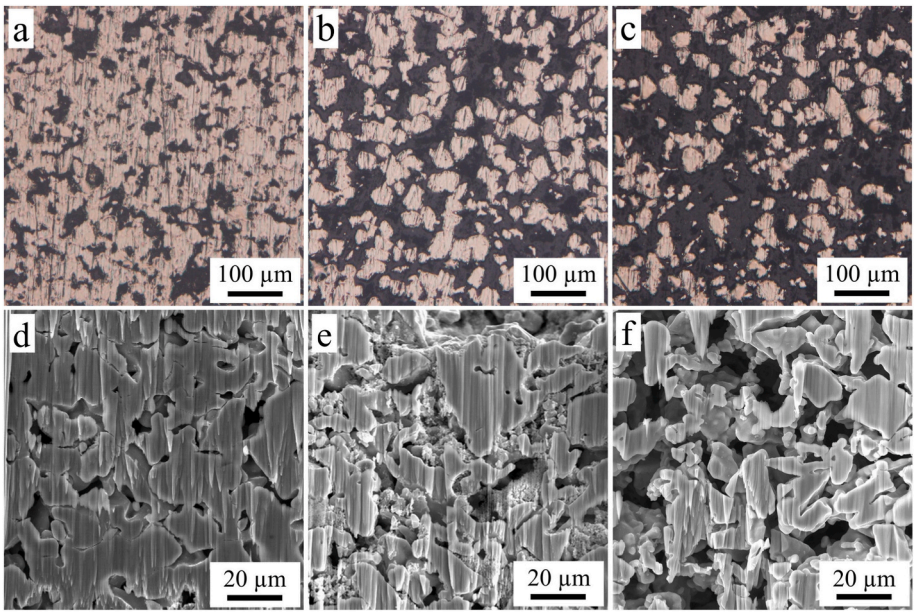


**Fig. 2.** OM (a–c) and SEM (d–f) images of (a,c) Ti-0.49, (b,d) Ti-0.37, and (c,f) Ti-0.32 samples.

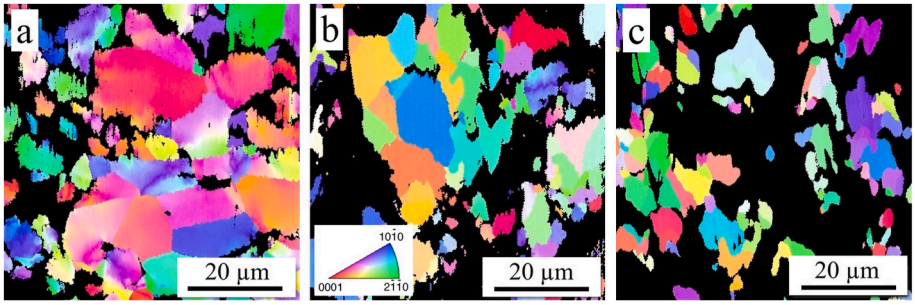


**Fig. 3.** EBSD images of (a) Ti-0.49, (b) Ti-0.37, and (c) Ti-0.32 samples.

density from 0.49 to 0.32, the grain size decreased from 10.6 to 5.1 μm. Although the grain size of Ti-0.32 was the smallest, the amount of grain boundaries inside the struts was the lowest among those of the three foams because the connectivity between the struts decreased significantly owing to the increased porosity level.

### 3.2. Mechanical properties

Fig. 4 shows examples of the engineering stress–strain curves obtained from sample Ti-0.37. Fig. 4a presents the compression curves detected at different initial strain rates, while Fig. 4b illustrates the reproducibility at 0.001 $s^{-1}$ strain rate. Up to approximately 0.2 strain, the stress–strain curves obtained at different strain rates are in good agreement. Subsequently, there is a stress drop and its magnitude varies significantly from sample to sample. However, this variation is not the result of the different strain rates since a similar difference in the stress drops can be observed for the same strain rate in Fig. 4b. In the next section, the combined application of AE and videos of the deformation process will reveal that the stress drop was caused by macroscopic fractures. This effect most probably occurs in areas in the samples in which the foam structure is the weakest owing to the high local porosity level and/or low contiguity of the struts. In samples with the same

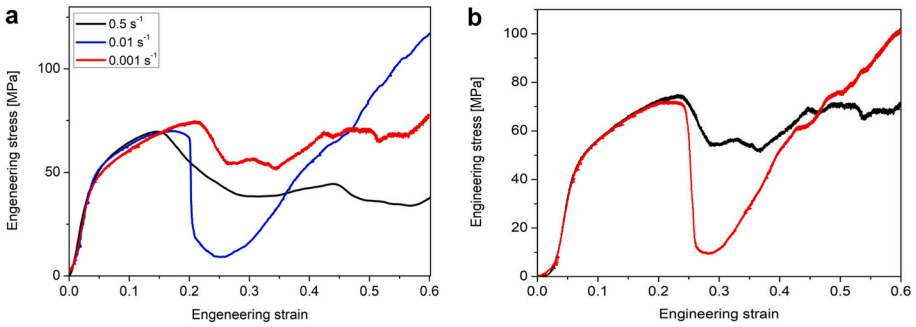


**Fig. 4.** (a) Engineering stress–strain curves of sample Ti-0.37 compressed at different initial strain rates. (b) Reproducibility of compression tests for sample Ti-0.37 at 0.001 $s^{-1}$ strain rate.

average relative density, the spatial distribution of the porosity and strut morphology may vary, thereby causing different stress drops in the compression curves. Therefore, in the study of the effect of porosity on the mechanical behavior, only the characteristic parameters of the stress–strain curve before the stress drop (i.e., up to approximately 0.2 strain for sample Ti-0.37) were determined. Since this part of the compression curve does not depend considerably on the strain rate (Fig. 4a), only the stress–strain data of the slowest, quasi-static deformation (0.001 $s^{-1}$ strain rate) were evaluated.

Fig. 5 shows typical engineering stress–strain curves of Ti foams with different relative densities compressed at 0.001 $s^{-1}$ strain rate; here, It is noted that the stress-strain curves for the Ti-0.37 foam shown in Figs. 4a and 5 were obtained on different samples and the two curves plotted in Figs. 4a and 5 for the Ti-0.37 foam material are shown together in Fig. 4b. Up to 0.4 strain, the compression curves can be classified into three stages. First, there is a quasi-linear stage, which is characteristic of porous materials. It is followed by a strain hardening region, which ends in a stress drop. After the stress drop, the stress–strain curve is serrated (i.e., it exhibits local fluctuations). Table 2 lists the Young's modulus as the slope of the first quasi-linear segment of the compression curve, the proof stress measured at 0.2% plastic strain, and the peak stress and strain at the stress drop (i.e., the maximum stress and strain before the stress drop, respectively) for the different relative densities. Since the strain rate did not cause significantly different mechanical properties, Table 2 shows the average values of the different strain rates. It can be seen that the Young's modulus, proof stress, and peak stress and strain at the stress drop decreased with increasing porosity. These trends are reasonable. The relationship between the relative density and relative proof stress and modulus will be analyzed quantitatively in the Discussion section of this paper.

### 3.3. Acoustic emission measurement

During the compression of the Ti foams, along with the compression curves, the AE response was detected, and the surface deformation was recorded with a video camera. The AE activity of the Ti foams with different densities was investigated at different initial strain rates. The evaluation of the AE parameters (i.e., the count rate and cumulative energy of the AE signals) indicated no changes in the deformation mechanisms with increasing strain rate in the investigated range (between 0.001 and 0.5 $s^{-1}$). Therefore, only the AE measurement conducted at 0.001 $s^{-1}$ initial strain rate was analyzed in detail. The lowest applied strain rate, 0.001 $s^{-1}$, was used for the evaluation of the AE measurements for two reasons: (i) it is easier to match the video images recorded on the surface deformation during the compression using 0.001 $s^{-1}$ with the AE measurements, and (ii) the signals of the different AE sources tend to overlap to a lesser degree.

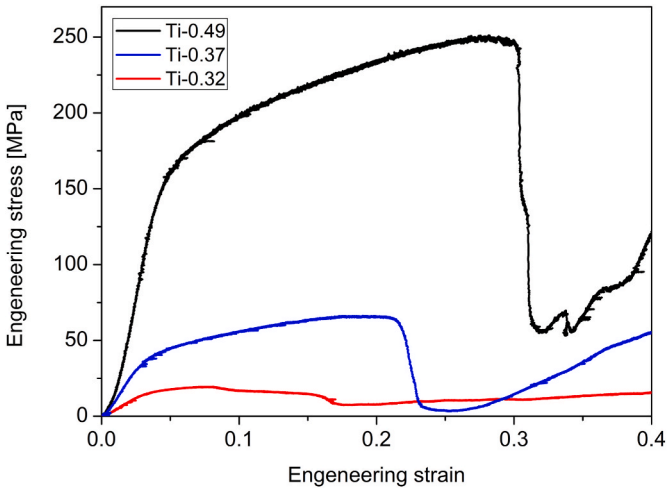


**Fig. 5.** Engineering stress–strain curves of Ti foams with different relative densities compressed at 0.001 $s^{-1}$ strain rate.

**Table 2**
Average Young's modulus, proof stress at 0.2% strain, and peak stress and maximum engineering strain before stress drop in compressive stress–strain curves. The errors were determined as the highest difference between the average and individual experimental values.

| Sample | Young's modulus (GPa) | 0.2% proof stress (MPa) | Peak stress (MPa) | Strain at stress drop (–) |
|---|---|---|---|---|
| Ti-0.49 | 5.95 ± 1.4 | 131 ± 8 | 278 ± 38 | 0.28 ± 0.06 |
| Ti-0.37 | 1.53 ± 0.09 | 39.3 ± 1.9 | 70.8 ± 1.4 | 0.17 ± 0.03 |
| Ti-0.32 | 0.69 ± 0.17 | 13.7 ± 0.9 | 20.6 ± 1.6 | 0.08 ± 0.02 |

Figs. 6–8 present the typical engineering stress–strain curves, measured AE activity, and snapshots of the video-recorded deformations of the Ti foams with three different densities. The deformation curves and AE response show some common characteristics. Some low-energy AE signals were measured even during the first quasi-linear stage. For each Ti foam, the count rate, which shows how many times the AE signal has exceeded the 0.07 mV threshold every 10 s, was below 100 $s^{-1}$. The count rate started to increase only close to the peak stress. However, it significantly increased only after the stress drop. After the stress drop, the AE parameters and features of the AE signal changed; the AE activity exhibited high-energy burst-type signals and serrated count rate curves with high local values. Changes in the cumulative energy curves are also visible; after the stress drop, there is a rapid increase in the cumulative energy. Both the count rate and cumulative energy curves present large stress drops. While the count rate curve always exhibits high count rates at the stress drop (Figs. 6–8), when the derivative of the stress–strain curve at the stress drop is not high (which indicates significant sudden events), there is no sharp increase in the cumulative energy curve (compare, e.g., Figs. 6 and 7).

In the strain hardening stage, there is a pronounced difference in the AE activity of the foams with different densities. For Ti-032, the low-AE activity region almost reaches the stress drop; some increase in the activity can be detected at only approximately 0.3%–0.5% strain before the stress drop. This value increases to approximately 2%–3% strain for Ti-0.37; for Ti-0.49, the AE activity starts to increase at approximately 10% strain before the stress drops. The sudden increases in the cumulative energy and count rate suggest that the origin of these AE signals is the formation and propagation of microcracks.

The recorded video showed that strain localization starts directly after the quasi-linear stage of the compression curve. This effect is particularly pronounced in the case of the Ti foam with 0.49 relative density; the changes in the reflection of the light due to the local plastic deformation are represented by bright spots on the specimen surface (Fig. 8). In addition, Fig. 8 shows that there are no bright spots on the sample surface at 0.04 strain (i.e., at the end of the quasi-linear stage), at 0.05 strain, there are bright spots on the lower part of the specimen; thus, the plastic deformation of this part of the sample has already started. Since the upper part of this sample remained unchanged at 0.05 strain, it can be concluded that strain localization occurs immediately after the quasi-linear stage of the deformation process. The video images and pictures in Figs. 6 and 7 show that the stress drops are due to the propagation of macroscopic cracks. When the stress drop was very large, a vertical crack appeared on the sample surface, and the specimen practically disintegrated during further compression.

## 4. Discussion

### 4.1. Effect of strain rate and porosity on deformation behavior

Fig. 4a shows that for the studied Ti foams, at the beginning of the plastic deformation, the compression stress–strain response did not

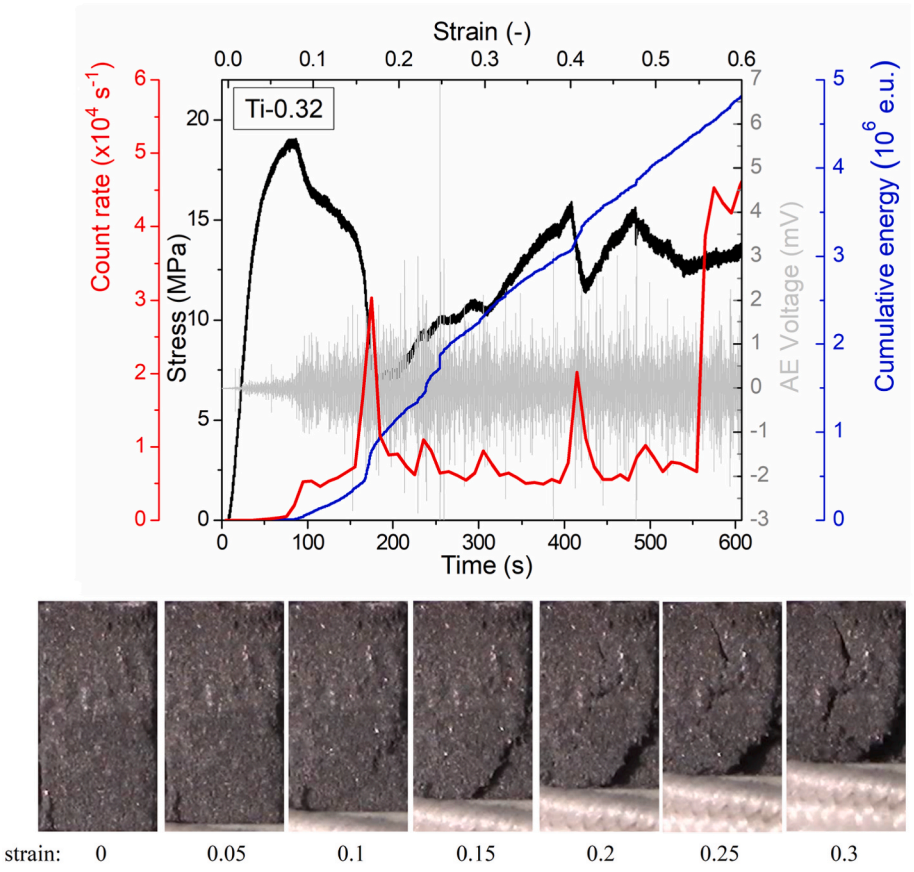


**Fig. 6.** Top: typical compressive engineering stress–strain curve of Ti foams with 0.32 relative density (black curve), measured AE signal (gray curve), and two AE parameters: the cumulative energy (blue curve) and count rate (red curve) of compression tests performed on Ti foam with different relative densities at 0.001 $s^{-1}$initial strain rate. Bottom: surfaces of foam samples at different strains. (For interpretation of the references to colour in this figure legend, the reader is referred to the Web version of this article.)

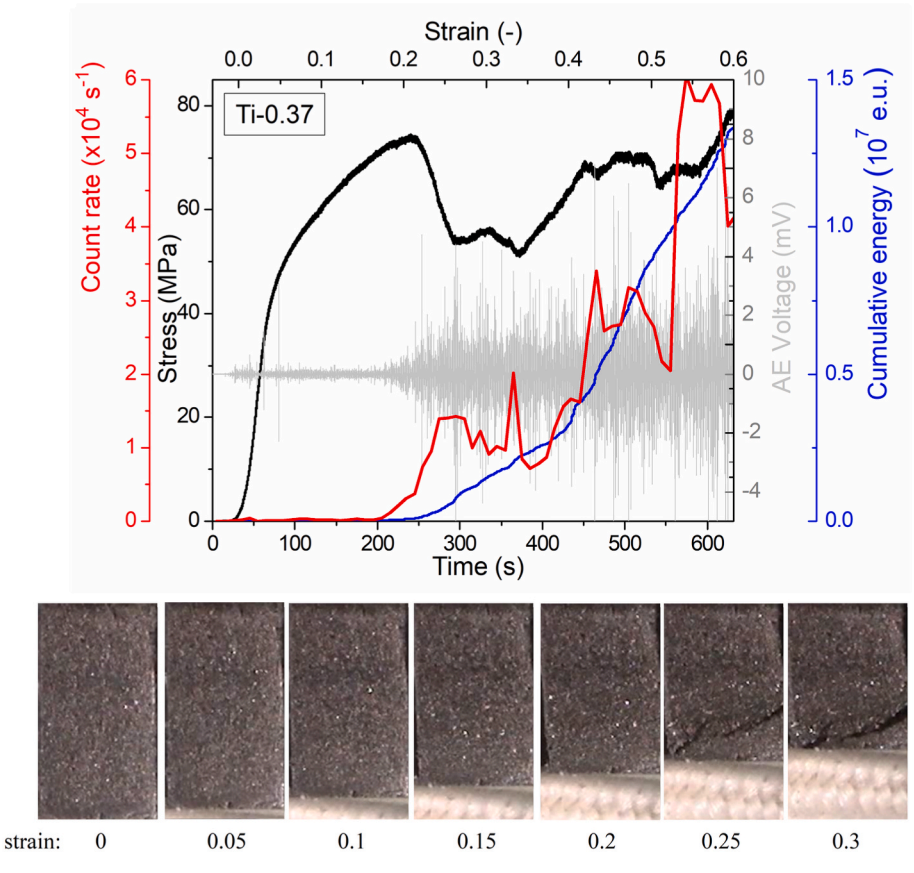


**Fig. 7.** Top: typical compressive engineering stress–strain curve of Ti foams with 0.37 relative density (black curve), measured AE signal (gray curve), and two AE parameters: the cumulative energy (blue curve) and count rate (red curve) of compression tests performed on Ti foam with different relative densities at 0.001 $s^{-1}$ initial strain rate. Bottom: surfaces of foam samples at different strains. (For interpretation of the references to colour in this figure legend, the reader is referred to the Web version of this article.)

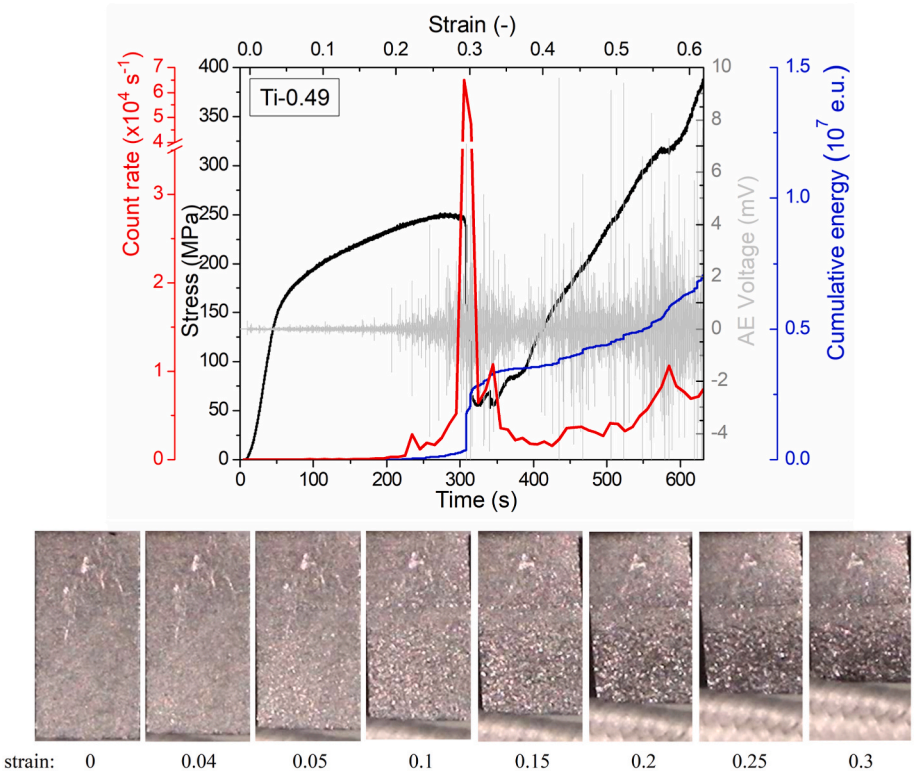


**Fig. 8.** Top: typical compressive engineering stress–strain curve of Ti foams with 0.49 relative density (black curve), measured AE signal (gray curve), and two AE parameters: the cumulative energy (blue curve) and count rate (red curve) of compression tests performed on Ti foam with different relative densities at 0.001 $s^{-1}$ initial strain. Bottom: surfaces of foam samples at different strains. (For interpretation of the references to colour in this figure legend, the reader is referred to the Web version of this article.)

depend significantly on the strain rate (at least between $10^{-3}$ and $5 \times 10^{-1}$ $s^{-1}$) if the reproducibility of the measurement is considered (Fig. 4b). A stress drop was observed at a strain between 0.08 and 0.28; it was associated with macrocracking, as revealed by the in-situ AE experiments and video. The strain related to this stress drop decreased with increasing porosity. This can be explained by the decreased connectivity between the struts with increasing porosity as can be seen from the SEM images in Fig. 2, Additionally, the thickness of the struts became narrower, which resulted in a reduced toughness of the Ti foam. Moreover, the plastic bending is then most likely to occur due to the narrower struts during deformation, which can lead to an premature failure. The present AE measurements also confirm that there is no significant difference between the deformation mechanisms at different strain rates between $10^{-3}$ and $5 \times 10^{-1}$ $s^{-1}$. It should be noted that the increased AE activity was observed even before the stress drop, which suggests the occurrence of microcracking; the most pronounced AE activity was detected for the samples with the highest relative density (Ti-0.49). The stress drop and subsequent increase in the stress due to densification vary from sample to sample according to Fig. 4. Although the stress–strain behavior prior to the stress drop does not depend significantly on the strain rate, the porosity has a considerable effect on this part of the compression curve (Fig. 5).

It is well known that α-phase Ti is deformed by dislocation slip, twinning, and grain boundary sliding and, at a higher strain, by fractures. According to the AE investigations of (pure) Ti, grain boundary sliding does not generate the AE signal [26]. Tanaka and Horiuchi showed that if the grain size is approximately 10 μm, the emission signals are continuous with low AE activity; in addition, no twinning takes place during deformation [27]. However, during the deformation of Ti with 55 μm grains, burst-type signals were measured in the AE experiment. These burst signals are attributed to twin formation [27]. Friesel and Carpenter discovered in AE experiments that the primary mechanism at the onset of plastic deformation in α-Ti is prismatic slip [26,28]. The average grain size of the investigated Ti foams was 5–10 μm; according to Ref. [27], there should be no AE signal originating from twinning and grain boundary sliding. As shown in Figs. 6–8, at the beginning of the deformation of the foam, the AE response exhibits low energy signals; thus, no twinning was found during the early deformation stage. Hong et al. investigated the AE activity of Mg foam [29]. They found that twinning takes place only at the beginning of the compression process, i.e., in the quasi-linear stage. With increasing strain, dislocation slip and bending of the Mg foam cell struts become the dominant deformation mechanisms. Figs. 6 and 7 suggest that in the case of Ti-0.32 and Ti-037, the low AE activity before the stress drop is due to the slip of dislocations and bending struts. However, in the case of Ti-049, the cumulative energy and count rates are an order of magnitude lower than those of Ti-0.32 and Ti-037 until approximately the end of the quasi-linear stage. Fig. 2 indicates that the dominance of dislocation slip over the other deformation mechanisms is probably the reason for this effect, whereas bending can also take place in Ti-0.32 and Ti-0.37 [29].

It should be noted that the deformation mechanisms examined by EBSD during compression of a freeze-cast Ti foam was already reported elsewhere [19]. The sample used in the former study had a relative density of 0.67 and was compressed up to the strain of 0.26. The analysis of the EBSD images showed that the misorientations between the neighboring regions inside the grains significantly increased, which was most likely caused by the formation of dislocations and their arrangement into low-angle grain boundaries (LAGBs). Indeed, complementary X-ray line profile analysis (XLPA) revealed an increase of the dislocation density by at least an order of magnitude when the strain increased to 0.26; however, twins were not observed by EBSD. This former investigation is in accordance with the results of AE in the present study, although AE was performed on samples with lower relative densities between 0.32 and 0.49.

### 4.2. *Relationship among relative density and mechanical properties*

For metallic foams, the relationship between the relative density and relative proof stress is usually described by a power law [24]:

$$\frac{\sigma_f}{\sigma_b} = C_\sigma \left(\frac{\rho_f}{\rho_b}\right)^{n_\sigma} \quad (1)$$

where $\sigma_f$ and $\sigma_b$ are the proof stress values of the foam and non-porous bulk material, respectively; $\rho_f$ and $\rho_b$ are the densities of the foam and non-porous bulk material, respectively. In this study, $\sigma_b = 480$ MPa and $\rho_b = 4.506$ gcm$^{-3}$ were used in the calculation of the relative proof stress and density, respectively. The prefactor $C_\sigma$ and exponent $n_\sigma$ depend on the deformation mechanism, which is influenced mainly by the amount, size, and morphology of pores. Fig. 9 shows a double logarithmic plot of the relative proof stress versus the relative density of the nine samples investigated in this study (black squares: six samples for each porosity level). A straight line was fitted to the points; $C_\sigma$ and $n_\sigma$ are 10.2 ± 1.1 and 5.0 ± 0.3, respectively. This very high exponent differs much from the values suggested by the models used for describing the deformation of metallic foams. Indeed, for the compression and GA models, $n_\sigma$ is 1 and 1.5, respectively [24]. To the best knowledge of the authors, there is no model in literature that predicts a value of 5 or similarly high values for $n_\sigma$. In addition to the results of the present study, Fig. 9 presents the relative stress values of Ti foams from literature as a function of the relative density. It should be noted that different characteristic stress values are presented for the different sample series in literature: in some papers, the yield strength is presented, whereas in others, the 0.2% proof stress or the plateau stress is used for the description of the porosity dependence of the mechanical strength of Ti foams. Nevertheless, for most of these sample series, $n_\sigma$ varies between 1 and 1.5, which agrees with the values of the frequently applied models. On the other hand, other freeze-cast Ti foam series exhibited exponent values that were as high as those of this study (see the data presented by Li et al. [21] in Fig. 9).

It is worth noting that in the calculation of the relative proof stress, a single $\sigma_b$ value was used for all the three relative densities. By contrast, the grain size in the foam material was different for the different porosities; this may influence the bulk proof stress according to the Hall–Petch equation [30]:

$$\sigma_b = \sigma_0 + kd^{-1/2} \quad (2)$$

where $\sigma_0$ is the friction stress (i.e., the proof stress without grain boundary strengthening), $d$ the grain size, and $k$ a constant that depends on the studied material. For Ti, $\sigma_0 = 182$ MPa and $k = 0.36$ MPa m$^{0.5}$ [31]. Table 1 shows that with increasing relative density from 0.32 to 0.49, the grain size increased from approximately 5 to 11 μm. In addition, in the foam with the highest porosity (Ti-0.32), the dimension of many struts is comparable with the grain size, at least in one direction (see the EBSD image in Fig. 3c). In the latter case, dislocations can glide in the grains without meeting boundaries, i.e., there is no Hall–Petch hardening effect despite the small grain size. For this material, the bulk proof stress must be low; the value corresponds to the friction stress in the Hall–Petch equation (approximately 182 MPa). For samples Ti-0.37 and Ti-0.49, the Hall–Petch equation yielded 324 and 293 MPa for $\sigma_b$, respectively. The respective relative proof stress versus the relative density is plotted in Fig. 10; the exponent of the straight fitting line decreased from 5.0 to 4.3. However, this value is still much higher than the exponents predicted with the usually applied models. It should be noted that there are different values for $\sigma_0$ and $k$ in literature in addition to those used in this study [32–34]. The variation in the Hall–Petch parameters can be attributed to the differences in the composition of Ti and the Hall–Petch evaluation procedure. For instance, a high oxygen content can influence $\sigma_0$ and $k$. Nevertheless, the Hall–Petch correction in the relative proof stress–relative density evaluation decreases the

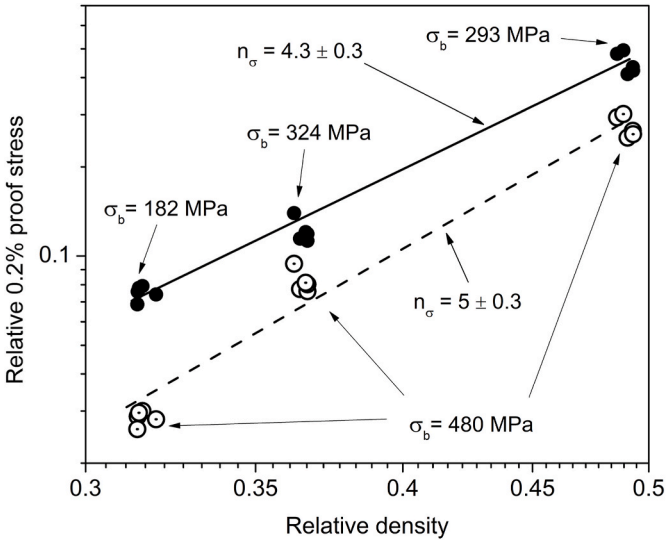


**Fig. 10.** Relative 0.2% compressive proof stress versus relative density on double logarithmic scale; measured proof stress is normalized with respect to the bulk proof stress corrected according to the Hall–Petch relationship based on the measured grain size (represented by the solid circles). This modified analysis decreases the power law exponent from $n_\sigma = 5.0$ to 4.3 *(please compare with Fig. 9)*.The open circles indicate the relationship between the relative stress and relative density without the application of the Hall-Petch correction.

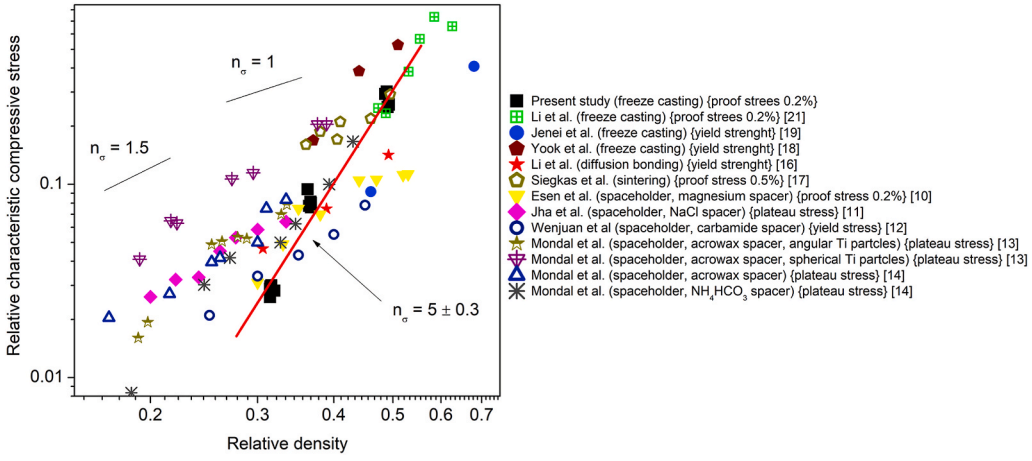


**Fig. 9.** Relative characteristic compressive stress (yield strength, proof stress, plateau stress) versus relative density of Ti foams on double logarithmic scale. The data originate from this study and literature. The characteristic compressive stress may correspond to the yield, proof, and plateau stresses of the different sample series, as indicated by the labels. In addition, the trend lines of some power law exponent values are shown.

power law exponent, regardless of the applied values of the Hall–Petch parameters.

Such as in the case of the proof stress, the correlation between the relative Young's modulus and relative density can be described by a power law [24]:

$$\frac{E_f}{E_b} = C_E\left(\frac{\rho_f}{\rho_b}\right)^{n_E} \quad (3)$$

where $E_f$ and $E_b$ are the Young's moduli of the foam and non-porous bulk material, respectively. Here, the prefactor and exponent are denoted as $C_E$ and $n_E$, respectively. Fig. 11 presents the relative Young's modulus versus the relative density on a double logarithmic scale. The nine points related to the Ti foams investigated in this study (three porosities and three samples for each porosity) are represented by solid black squares in the plot. The values of $C_E$ and $n_E$ obtained from the parameters of the straight line fitted to the data in Fig. 11 are 1.3 ± 1.2 and 4.6 ± 0.3, respectively. This exponent is very large compared to the values determined for the most frequently used compression and GA models ($n_E = 1$ and 2, respectively [24]). Fig. 11 also shows data series from literature. For most of these samples, the trends are in accordance with either the compression or the GA model. However, there are other sample series (e.g., Refs. [10,13,15]), the exponents of which are approximately 4–5; thus, they are similar to those of the studied Ti foams.

The experimentally obtained very high power law for the dependence of the relative proof stress and relative elastic modulus on the relative density cannot be explained by any of the models presented in literature. Even if the density corrections of the GA model (due to the existence of nodes) are considered [24], the power law exponent of the relative Young's modulus and the relative proof stress as a function of the relative density increase to 2.3 and 3, respectively; these values are still well below the fitted values. However, a change in the deformation mechanism may have occurred owing to changes in the porosity, which may have led to the unusual power law exponent. Therefore, in the following chapter, we determine whether a transition between the different structural models can yield a high exponent of approximately 4–5 for the dependence of the proof stress and elastic modulus on the relative density.

Fig. 12 schematically shows the relative proof stress versus the relative density for the compression and GA models on a double logarithmic scale. Each model is represented by a strip because $C_\sigma$ may vary although the exponent is fixed. According to literature, for the compression model, $n_\sigma = 1$, and $C_\sigma$ varies between 0.4 and 0.5 [35]. For the GA model, $n_\sigma = 1.5$, and $C_\sigma$ varies between 0.25 and 0.35 [34]. The blue and red lines in Fig. 12 represent model transitions yielding the

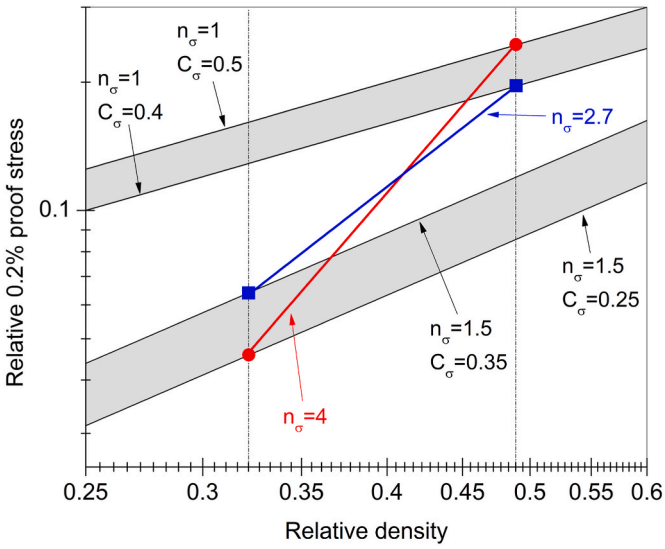


**Fig. 12.** Relative 0.2% compressive proof stress versus relative density on double logarithmic scale for compression ($n_\sigma = 1$) and GA ($n_\sigma = 1.5$) models with a reasonable range of $C_\sigma$ values. The blue and red lines indicate the lowest and highest possible exponents that can be observed for model transitions in the relative density range between 0.32 and 0.49. (For interpretation of the references to colour in this figure legend, the reader is referred to the Web version of this article.)

lowest and highest possible exponents for the relative density range investigated in this study (0.32–0.49). Evidently, the model transition (i.e., the change of the deformation mechanism) due to the increasing relative density can yield a power law exponent $n_\sigma$ between 2.7 and 4 in the proof stress–density relationship. This means that the model transition can explain the experimentally observed value of $n_\sigma$ (4.3 ± 0.3). The fact that the AE activity was much lower for the highest density foam (with the most material) than those for Ti-0.37 and Ti-0.32 also suggests a change in the deformation mechanism.

Such as for the proof stress, the effect of the model transition on the power law exponent of the relative Young's modulus versus the relative density relationship was studied. Fig. 13 presents schematics of the compression and GA models. For the compression model, $n_E = 1$, and $C_E$ varies between 0.4 and 0.5 [34]. For the GA model, $n_E = 2$, and according to literature, $C_E$ varies in a relatively wide range (0.1–1) [11, 35]. This very broad $C_E$ range is probably not caused by the structural

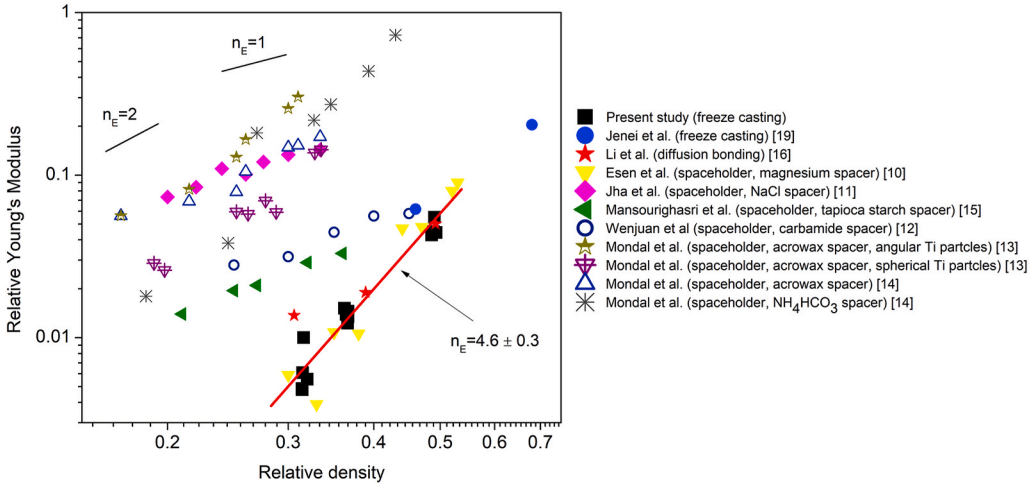


**Fig. 11.** Relative Young's modulus versus relative density of Ti foams on double logarithmic scale. The data originate from this study and literature. In addition, the trend lines for some power law exponent values are shown.

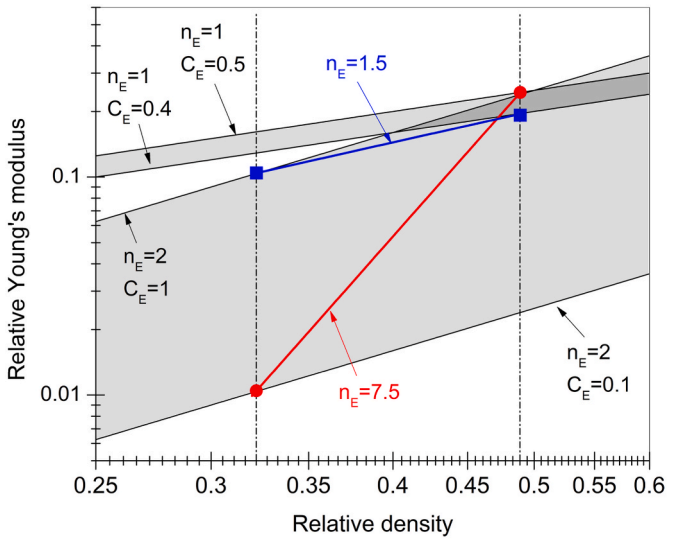


**Fig. 13.** Relative Young's modulus versus relative density on double logarithmic scale for the compression ($n_E$ =1) and GA ($n_E$ =2) models with a reasonable range of $C_E$ values. The blue and red lines indicate the lowest and highest possible exponent that can be observed for model transitions in the relative density range between 0.32 and 0.49. (For interpretation of the references to colour in this figure legend, the reader is referred to the Web version of this article.)

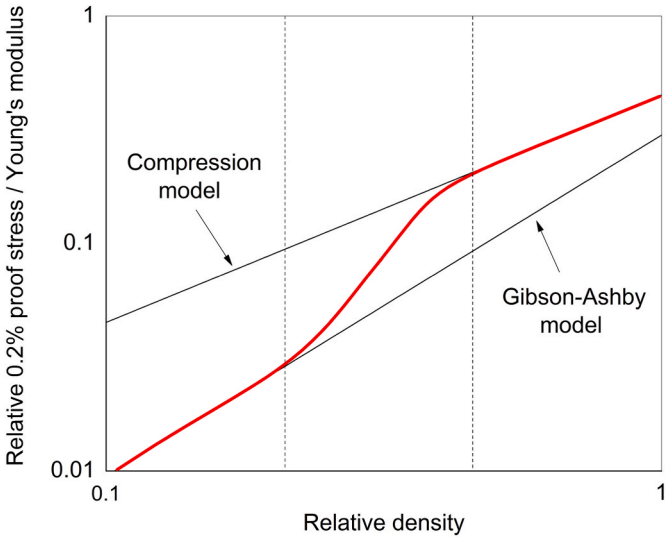


**Fig. 14.** Transition between the compression and GA models of the relative 0.2% compressive proof stress or Young's modulus versus the relative density.

differences among the different sample series; the cause is rather the uncertainty in the determination of Young's modulus. Indeed, the initial elastic part of the compression curves is often not perfectly straight (Fig. 5); therefore, the value of Young's modulus depends on the region selected for the evaluation. Most probably, this uncertainty is the reason for the highly scattered experimentally determined relative elastic moduli in Fig. 11. Owing to the very different probable values of $C_E$ for the GA model, the transition between the two models results in a wide $n_E$ range (1.5–7.5). The experimentally measured power law exponent (approximately 5) falls within this range, i.e., the model transition can be a possible explanation for the high $n_E$. It should be noted that in the case of the relative Young's modulus, a power law exponent of approximately 5 can also be obtained if the GA model remains valid for 0.32–0.49 relative density and if only $C_E$ increases within the wide range (0.1–1). However, the prefactor $C_\sigma$ of the proof stress is less uncertain; therefore, the high value of $n_\sigma$ (4.3) can only be explained based on the model transition.

It should also be noted that the high power law exponents obtained for the density dependence of the proof stress and elastic modulus are surely not valid for the whole range of the relative density achievable with foam processing methods (0.11–0.9 [14,17]). Most probably, the GA and compressive models work well for low and high relative densities, respectively, and the power law with a high exponent describes only the transition region, as schematically illustrated in Fig. 14.

Fig. 15 shows a descriptive structural model for the change of the deformation mechanism from a dominant compression to bending of the struts. In this model, the Ti foams mainly consist of spherical particles in accordance with the SEM images taken on our samples. When these spheres are assumed to be arranged into a simple cubic structure as shown in Fig. 15a, the relative density is 0.52 that is only slightly higher than the highest value in the present study (0.49). For this simply assumed structure, a vertical load mainly results in compression of the struts. If we remove spheres from the structure in a way described in Fig. 15b, the relative density significantly decreased down to 0.26. This structural change can be easily understood if a cube containing eight simple cubic cells is considered as a structural unit in Fig. 15a. It is then assumed that the six spheres in the centers of the faces and one sphere in the cube center are removed, yielding the structure shown in Fig. 15b. It is noted that the centers of the hollow cubes are shifted horizontally as illustrated in Fig. 15b. For the latter structure with a low relative density, the vertical load causes bending of the horizontal struts as illustrated by the dashed curves in Fig. 15b; in other words, there is a transition of the dominant deformation mechanism from compression to bending when the relative density decreased from 0.52 to 0.26. It is noted with care that Fig. 15 describes only an illustrative example of the change of deformation mechanism and does not provide a precise theoretical mechanism explanation, as the actual Ti foam microstructure is considerably less ordered than the constructed model proposed in Fig. 15.

## 5. Conclusions

The effects of the porosity and strain rate on the compression behavior of freeze-cast Ti foams were studied. The following conclusions were drawn from the results:

1. Considerable strain hardening was observed in the first stage of the plastic deformation process; the process was independent of the porosity level and applied strain rate. Subsequently, a stress drop occurred, which was associated with extensive cracking, as revealed by in-situ AE experiments. Moreover, microcracking was detected in the AE experiments before the maximum stress was reached for the highest relative density (0.49).
2. Before the stress drop, there was no considerable effect of the rate of compression on the stress–strain behavior, even when the initial strain rate varied between 0.001 and 0.5 $s^{-1}$. The AE results also indicate that the deformation mechanisms were not influenced by the strain rate.
3. Both the relationships of the Young's modulus and yield strength with the relative density are well described by a power law with an exponent of approximately 4–5. This value is much higher than the exponents suggested by already proposed deformation models for metallic foams. According to the results, the high exponent originates from a transition from the compression to the bending mode with increasing porosity. In addition, for the yield strength, the high exponent of approximately 5 can be reduced to approximately 4.3 if the Hall–Petch effect of the grain size in the struts is considered.
4. With increasing porosity, the strain decreased significantly until the stress drop owing to the lower number of neighbor contacts, which weakens the structure.

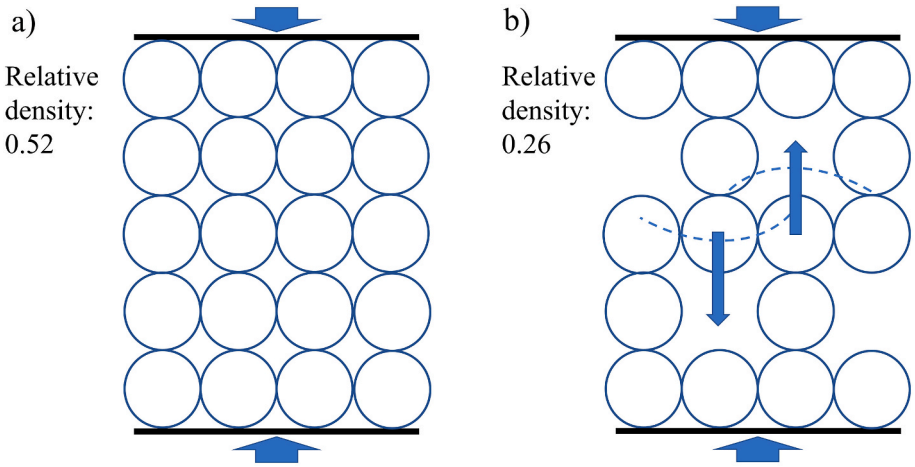


**Fig. 15.** A schematic of structural models for foams with (a) high and (b) low relative densities, which were calculated from the 3D layout of the models. The spheres represent the particles constructing the foam. For the higher relative density, the particles are assumed to be arranged in a simple cubic structure, while for the lower relative density, the spheres are arranged lying along the edges of cubes with a length equal to twice of the sphere diameter.

## CRediT authorship contribution statement

**Péter Jenei:** Methodology, Formal analysis, Visualization, Data curation, Writing – original draft, Writing – review & editing. **Csilla Kádár:** Methodology, Formal analysis, Visualization, Data curation, Validation, Writing – original draft, Writing – review & editing. **Ábel Szabó:** Methodology, Validation, Formal analysis. **Sun–Mao Hung:** Conceptualization, Methodology, Resources, Investigation, Funding acquisition. **Chia–Jung Kuo:** Conceptualization, Methodology, Resources, Investigation, Funding acquisition. **Heeman Choe:** Conceptualization, Methodology, Validation, Funding acquisition, Writing – original draft, Writing – review & editing. **Jenő Gubicza:** Methodology, Validation, Formal analysis, Writing – original draft, Writing – review & editing.

## Declaration of competing interest

The authors declare that they have no known competing financial interests or personal relationships that could have appeared to influence the work reported in this paper.

## Data availability

Data will be made available on request.

## Acknowledgment

The research reported in this paper is a part of project no. BME-NVA-02, implemented with the support provided by the Ministry of Innovation and Technology of Hungary from the National Research, Development and Innovation Fund, financed under the TKP2021 funding scheme. HC acknowledges support from CellMobility Inc.

## References

[1] K.L. Scotti, D.C. Dunand, Freeze casting - a review of processing, microstructure and properties via the open data repository, FreezeCasting.net, Prog. Mater. Sci. 94 (2018) 243–305, https://doi.org/10.1016/j.pmatsci.2018.01.001.
[2] R. Goodall, A. Mortensen, Porous metals, Physical Metallurgy (2014) 2399–2595, https://doi.org/10.1016/b978-0-444-53770-6.0. Porous Metals.
[3] Y. Conde, J.-F. Despois, R. Goodall, A. Marmottant, L. Salvo, C. San Marchi, A. Mortensen, Replication processing of highly porous materials, Adv. Eng. Mater. 8 (9) (2006) 795–803, https://doi.org/10.1002/adem.200600077.
[4] Y. Higuchi, Y. Ohashi, H. Nakajima, Biocompatibility of lotus-type stainless steel and titanium in alveolar bone, Adv. Eng. Mater. 8 (9) (2006) 907–912, https://doi.org/10.1002/adem.200600124.
[5] T. Matsushita, S. Fujibayashi, T. Kokubo, 4 - Titanium Foam for Bone Tissue Engineering, Elsevier Ltd, 2017, https://doi.org/10.1016/B978-0-08-101289-5.00004-4.
[6] A. Salimon, Y. Bréchet, M.F. Ashby, A.L. Greer, Potential applications for steel and titanium metal foams, J. Mater. Sci. 40 (22) (2005) 5793–5799, https://doi.org/10.1007/s10853-005-4993-x.
[7] D.C. Dunand, Processing of titanium foams, Adv. Eng. Mater. 6 (6) (2004) 369–376, https://doi.org/10.1002/adem.200405576.
[8] L. Yang, O. Harrysson, H. Cormier D, D. Cormier, A comparison of bending properties for cellular core sandwich panels, Msa 4 (8) (2013) 471–477, https://doi.org/10.4236/msa.2013.48057.
[9] J. Zhang, G. Lu, Z. You, Large deformation and energy absorption of additively manufactured auxetic materials and structures: a review, Compos. B Eng. vol. 201 (2020) 108340, https://doi.org/10.1016/j.compositesb.2020.
[10] Z. Esen, Ş. Bor, Processing of titanium foams using magnesium spacer particles, Scripta Mater. 56 (5) (2007) 341–344, https://doi.org/10.1016/j.scriptamat.2006.11.010.
[11] N. Jha, D.P. Mondal, J. Dutta Majumdar, A. Badkul, A.K. Jha, A.K. Khare, Highly porous open cell Ti-foam using NaCl as temporary space holder through powder metallurgy route, Mater. Des. 47 (2013) 810–819, https://doi.org/10.1016/j.matdes.2013.01.005.
[12] N. Wenjuan, B. Chenguang, Q. GuiBao, W. Qiang, Processing and properties of porous titanium using space holder technique, Mater. Sci. Eng. 506 (2009) 148–151, https://doi.org/10.1016/j.msea.2008.11.022.
[13] D.P. Mondal, M. Patel, H. Jain, A.K. Jha, S. Das, R. Dasgupta, The effect of the particle shape and strain rate on microstructure and compressive deformation response of pure Ti-foam made using acrowax as space holder, Mater. Sci. Eng., A 625 (2015) 331–342, https://doi.org/10.1016/j.msea.2014.12.001.
[14] D.P. Mondal, M. Patel, S. Das, A.K. Jha, H. Jain, G. Gupta, S.B. Arya, Titanium foam with coarser cell size and wide range of porosity using different types of evaporative space holders through powder metallurgy route, Mater. Des. 63 (2014) 89–99, https://doi.org/10.1016/j.matdes.2014.05.054.
[15] A. Mansourighasri, N. Muhamad, A.B. Sulong, Processing titanium foams using tapioca starch as a space holder, J. Mater. Process. Technol. 212 (1) (2012) 83–89, https://doi.org/10.1016/j.jmatprotec.2011.08.008.
[16] F. Li, J. Li, T. Huang, H. Kou, L. Zhou, Compression fatigue behavior and failure mechanism of porous titanium for biomedical applications, J. Mech. Behav. Biomed. Mater. 65 (2017) 814–823, https://doi.org/10.1016/j.jmbbm.2016.09.035.
[17] P. Siegkas, N. Petrinic, V.L. Tagarielli, Measurements and micro-mechanical modelling of the response of sintered titanium foams, J. Mech. Behav. Biomed. Mater. 57 (2016) 365–375.
[18] S.W. Yook, B.H. Yoon, H.E. Kim, Y.H. Koh, Y.S. Kim, Porous titanium (Ti) scaffolds by freezing TiH2/camphene slurries, Mater. Lett. 62 (30) (2008) 4506–4508, https://doi.org/10.1016/j.matlet.2008.08.010.
[19] P. Jenei, H. Choi, A. Tóth, H. Choe, J. Gubicza, Mechanical behavior and microstructure of compressed Ti foams synthesized via freeze casting, J. Mech. Behav. Biomed. Mater. 63 (2016) 407–416, https://doi.org/10.1016/j.jmbbm.2016.07.012.
[20] S.W. Yook, H.E. Kim, Y.H. Koh, Fabrication of porous titanium scaffolds with high compressive strength using camphene-based freeze casting, Mater. Lett. 63 (17) (2009) 1502–1504, https://doi.org/10.1016/j.matlet.2009.03.056.
[21] J.C. Li, D.C. Dunand, Mechanical properties of directionally freeze-cast titanium foams, Acta Mater. 59 (1) (2011) 146–158, https://doi.org/10.1016/j.actamat.2010.09.019.
[22] Y. Chino, D.C. Dunand, Directionally freeze-cast titanium foam with aligned, elongated pores, Acta Mater. 56 (1) (2008) 105–113, https://doi.org/10.1016/j.actamat.2007.09.002.

[23] H. Choi, S. Shil'ko, J. Gubicza, H. Choe, Study of the compression and wear-resistance properties of freeze-cast Ti and Ti–5W alloy foams for biomedical applications, J. Mech. Behav. Biomed. Mater. 72 (2017) 66–73, https://doi.org/10.1016/j.jmbbm.2017.04.020.
[24] L.G. Gibson, M.F. Ashby, Cellular Solids, Structures and Properties, second ed., Cambridge University Press, 1997.
[25] H. Choi, O.H. Kim, M. Kim, H. Choe, Y.H. Cho, Y.E. Sung, Next-generation polymer-electrolyte-membrane fuel cells using titanium foam as gas diffusion layer, ACS Appl. Mater. Interfaces 6 (2014) 7665–7671, https://doi.org/10.1021/am500962h.
[26] M.A. Friesel, S.H. Carpenter, An inverted strain rate dependence of the acoustic emission generated during the deformation of high purity α-Ti, Mater. Sci. Eng. 68 (1) (1984) 107–111, https://doi.org/10.1016/0025-5416(84)90248-9.
[27] H. Horiuchi R, R. Horiuchi, Scripta Metallurgica, 7, in: Acoustic Emission Due to Deformation Twinning in Titanium and Ti-6Al-4V Alloy, vol. 9, Pergamon Press, Inc, 1975, pp. 777–780.
[28] M.A. Friesel, S.H. Carpenter, Determination of the sources of acoustic emission generated during the deformation of titanium, Mta 15 (10) (1984) 1849–1853, https://doi.org/10.1007/BF02664898.
[29] K. Hong, H. Park, Y. Kim, M. Knapek, P. Minárik, K. Máthis, A. Yamamoto, H. Choe, Mechanical and biocorrosive properties of magnesium-aluminum alloy scaffold for biomedical applications, J. Mech. Behav. Biomed. Mater. 98 (2019) 213–224, https://doi.org/10.1016/j.jmbbm.2019.06.022.
[30] E.O. Hall, The deformation and ageing of mild steel: III discussion of results, Proc. Phys. Soc. B 64 (9) (1951) 747–753. https://doi:10.1088/0370-1301/64/9/303.
[31] P. Luo, D.T. McDonald, W. Xu, S. Palanisamy, M.S. Dargusch, K. Xia, A modified Hall-Petch relationship in ultrafine-grained titanium recycled from chips by equal channel angular pressing, Scripta Mater. 66 (10) (2012) 785–788, https://doi.org/10.1016/j.scriptamat.2012.02.008.
[32] G.S. Dyakonov, S. Mironov, I.P. Semenova, R.Z. Valiev, S.L. Semiatin, Microstructure evolution and strengthening mechanisms in commercial-purity titanium subjected to equal-channel angular pressing, Mater. Sci. Eng., A 701 (2017) 289–301, https://doi.org/10.1016/j.msea.2017.06.079.
[33] P. Luo, D.T. McDonald, S.M. Zhu, S. Palanisamy, M.S. Dargusch, K. Xia, Analysis of microstructure and strengthening in pure titanium recycled from machining chips by equal channel angular pressing using electron backscatter diffraction, Mater. Sci. Eng., A 538 (2012) 252–258, https://doi.org/10.1016/j.msea.2012.01.039.
[34] G.S. Dyakonov, S. Mironov, I.P. Semenova, R.Z. Valiev, Chapter 7 - Strengthening Mechanisms and Super-strength of Severely Deformed Titanium, Elsevier Inc., 2019, https://doi.org/10.1016/B978-0-12-814599-9.00007-9.
[35] J. Gubicza, P. Jenei, K. Nam, C. Kádár, H. Jo, H. Choe, Compressive behavior of Cu-Ni alloy foams: effects of grain size, porosity, pore directionality, and chemical composition, Mater. Sci. Eng., A 725 (2018) 160–170, https://doi.org/10.1016/j.msea.2018.04.018.